US Department of Energy Publications

U.S. Department of Energy

2011

Roaming radicals in the thermal decomposition of dimethyl ether: Experiment and theory

R. Sivaramakrishnan
Argonne National Laboratory, Argonne, IL

J. Michael
Argonne National Laboratory, Argonne, IL

A. Wagner
Argonne National Laboratory, Argonne, IL

R. Dawes
Missouri University of Science and Technology, Rolla, MO

A. Jasper
Sandia National Laboratories, Livermore, CA

See next page for additional authors

Authors

R. Sivaramakrishnan, J. Michael, A. Wagner, R. Dawes, A. Jasper, L. Harding, Y. Georgievskii, and S. Klippenstein

Roaming radicals in the thermal decomposition of dimethyl ether: Experiment and theory

R. Sivaramakrishnan [a], J.V. Michael [a,*], A.F. Wagner [a,*], R. Dawes [b,c], A.W. Jasper [c], L.B. Harding [a], Y. Georgievskii [a], S.J. Klippenstein [a]

[a] Chemical Sciences and Engineering Division, Argonne National Laboratory, Argonne, IL 60439, USA
[b] Missouri University of Science and Technology, Rolla, MO 65409, USA
[c] Combustion Research Facility, Sandia National Laboratories, Livermore, CA 94551, USA

ABSTRACT

The thermal dissociation of dimethyl ether has been studied with a combination of reflected shock tube experiments and ab initio dynamics simulations coupled with transition state theory based master equation calculations. The experiments use the extraordinary sensitivity provided by H-atom ARAS detection with an unreversed light source to measure both the total decomposition rate and the branching to radical products versus molecular products, with the molecular products arising predominantly through roaming according to the theoretical analysis. The experimental observations also provide a measure of the rate coefficient for $H + CH_3OCH_3$. An evaluation of the available experimental results for $H + CH_3OCH_3$ can be expressed by a three parameter Arrhenius expression as,

$$k = 6.54 \times 10^{-24} T^{4.13} \exp(-896/T) \text{ cm}^3 \text{ molecule}^{-1} \text{ s}^{-1} (273 - 1465 \text{ K})$$

The potential energy surface is explored with high level ab initio electronic structure theory. The dynamics of roaming versus radical formation is studied with a reduced dimensional trajectory approach. The requisite potential energy surface is obtained from an interpolative moving least squares fit to wide-ranging ab initio data for the long-range interactions between methyl and methoxy. The predicted roaming and radical micro-canonical fluxes are incorporated in a master equation treatment of the temperature and pressure dependence of the dissociation process. The tight (i.e., non-roaming) transition states leading to a variety of additional molecular fragments are also included in the master equation analysis, but are predicted to have a negligible contribution to product formation. The final theoretical results reliably reproduce the measured dissociation rate to radical products reported here and are well reproduced over the 500–2000 K temperature range and the 0.01–300 bar pressure range by the following modified Arrhenius parameters for the Troe falloff format:

$$k_{1,\infty}(T) = 2.33 \times 10^{19} T^{-0.661} \exp(-42345/T) \text{ s}^{-1}$$
$$k_{1,0}(T) = 2.86 \times 10^{35} T^{-11.4} \exp(-46953/T) \text{ cm}^3 \text{ molecule}^{-1} \text{ s}^{-1}$$
$$F_{cent}(T) = \exp(-T/880)$$

The experimentally observed branching ratio of 0.19 ± 0.07 provides a direct measure of the contribution from the roaming radical mechanism. The theoretical analysis predicts a much smaller roaming contribution of 0.02.

© 2010 The Combustion Institute. Published by Elsevier Inc. All rights reserved.

1. Introduction

The simplest of the ethers, dimethyl ether (DME), is a synthetic fuel produced commonly from syngas (CO, H_2) and also from a variety of other feedstocks such as coal, natural gas, biomass, and blends of these. When DME burns it is smokeless, and it is therefore a favorable replacement candidate for diesel fuel from an emissions perspective. In addition to being a potential diesel fuel

replacement, DME can also be used as (1) a fuel in gas turbines for power generation, (2) an LPG substitute, (3) a hydrogen source for fuel cells, and (4) as a feedstock for chemicals [1]. Recent interest in DME as an alternative fuel and as a potential additive has spurred a number of combustion studies that have been highlighted in a special issue [2].

Thermal decomposition plays a significant role in the combustion kinetics of DME [3]. In all previous experimental studies [4–10] the thermal decomposition of CH_3OCH_3 is presumed to undergo C–O bond fission through R1,

$$CH_3OCH_3 \rightarrow CH_3 + CH_3O \qquad (R1)$$

However, recent theoretical studies [11] suggest the ubiquity of roaming radical processes in a variety of molecular systems. For DME, the roaming radical mechanism, if present, will lead to the formation of molecular products, CH_4 and CH_2O, through R2,

$$CH_3OCH_3 \rightarrow CH_3 \cdots OCH_3 \rightarrow OCH_3 \cdots CH_3 \rightarrow CH_4 + CH_2O \qquad (R2)$$
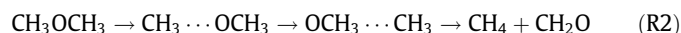
The branching between radical (R1) and molecular (R2) products might be expected to have a significant impact on the combustion properties for DME.

Early studies on roaming radical mechanisms considered the photodissociation of small molecular systems. For example, in formaldehyde it was shown that during the process of C–H bond fission some of the departing H-atoms can roam around the HCO moiety at long-range and then abstract a hydrogen atom with no further activation energy to produce $H_2 + CO$ [12]. Subsequent experimental and theoretical studies on acetaldehyde photodissociation demonstrated the presence of an analogous process with a roaming CH_3 radical to give $CH_4 + CO$ [13–15].

The branching to a roaming channel in a thermal dissociation was first identified in a combination of experimental and theoretical studies [16,17] on acetaldehyde. DME represents another potential candidate for an important roaming radical channel in a thermal dissociation. A preliminary scan of the DME potential energy surface reveals that the saddle point for the roaming process ($CH_3 \cdots OCH_3 \rightarrow OCH_3 \cdots CH_3$) is ~2 kcal/mol below the C–O bond fission asymptote. For CH_3CHO, the roaming radical transition state was ~1 kcal/mol below the C–C bond fission asymptote [17]. Consequently, one might expect in DME a similar if not larger contribution from the roaming radical mechanism than in CH_3CHO.

In this work, we employ a combination of experimental measurements and theoretical analyses in a detailed study of the roaming fraction for the thermal decomposition of DME. This analysis is closely related to the prior study of the thermal dissociation of acetaldehyde [16,17]. The experimental component of this work employs the reflected shock-tube technique with a high sensitivity H-atom Atomic Resonance Absorption Spectroscopy (ARAS) detection scheme to minimize secondary reactions and determine absolute yields of products. At high temperatures, CH_3O instantaneously dissociates to $H + CH_2O$, and, therefore, temporal H-atom measurements are good indicators for the rate of R1.

One aspect of the theoretical analysis involves ab initio transition state theory based master equation calculations of the rate coefficients for the various decomposition processes. This analysis indicates that the channels leading to $H_2 + CH_3OCH$, $H + CH_3OCH_2$, and $^1CH_2 + CH_3OH$ are kinetically insignificant. As discussed below, the present experimental measurements then directly provide the branching between the C–O bond dissociation channel (R1) and the roaming channel (R2).

The primary focus of the theoretical analysis is on the direct calculation of the roaming fraction as a complement to the experimental measurements of this quantity. These calculations are carried out with a reduced dimensional trajectory (RDT) approach as described in Ref. [17]. The RDT calculations require a six-dimensional potential energy surface describing the interaction between rigid CH_3 and CH_3O radicals for arbitrary orientations and separation. Here, this potential energy surface is generated from a novel application of the interpolative moving least squares (IMLS) fitting approach [18], with the underlying ab initio data obtained from multi-reference second order perturbation theory (CASPT2).

The experimental work adds significantly to the database for DME decomposition. The majority of the prior DME thermal decomposition studies were carried out in flow reactors [4–8]. These studies used large initial concentrations of fuel, and, therefore, the thermal decomposition rate coefficients relied heavily on detailed chemical kinetics modeling. In order to better characterize the high-temperature thermal decomposition rates, two recent studies have been carried out using shock tubes. The Fernandes et al. [9] study used H-atom ARAS as the diagnostic for measuring rate coefficients for R1. By contrast, the Cook et al. [10] study used mixtures of DME in excess O_2 with OH-absorption as the diagnostic. The resulting H-atoms from CH_3O decomposition react with excess O_2 to form OH through the chain branching reaction, $H + O_2 \rightarrow OH + O$, and therefore, the OH-temporal profiles can then be used to obtain rate constants for R1.

Both new studies employed analytical techniques that allowed the use of much lower initial concentrations of DME than earlier studies [4–8]; however, they still need to use a chemical kinetic model to extract rate coefficients for R1. Even the H-atom ARAS study of Fernandes et al. [9], with the lowest initial DME concentrations of any published DME kinetics experiment, still used relatively large initial concentrations. As a result, one secondary reaction, namely $H + CH_3OCH_3 \rightarrow$ products, had a major effect on the long time values of [H]. These authors were able to specify rate constants for this reaction through modeling, and subsequently, also for the thermal decomposition.

Not only are all prior DME kinetics studies complicated by secondary reaction perturbations, but, more importantly for this study, absolute yields for various thermal decomposition channels could not be directly measured. In contrast, the present work uses a higher sensitivity H-atom ARAS detection scheme to minimize secondary reactions, and this allows determinations for absolute yields of products. The resonance light source used in this laboratory is unreversed, giving an increase of ~5–10 in sensitivity over that used by Fernandes et al. [9], who also used the ARAS technique but with a substantially reversed resonance light source [19]. As in earlier work [20], we show that this unreversed source allows experiments to be performed under pseudo-first order conditions; i.e., with no secondary reaction interferences.

We also extend these ultra-dilute pseudo-first order studies to experiments with roughly the same $[CH_3OCH_3]_0$ as Fernandes et al. [9]. These higher concentration experiments expand our rate constant database for DME decomposition to lower-T, and allow for the determination of rate constants for $H + CH_3OCH_3$ via the modeling of the temporal H-atom profiles. The measurements for the H + DME reaction extend the experimental rate database for that reaction to higher-T than the recent measurements of Takahashi et al. [21].

2. Experiment

The present experiments were performed with the reflected shock-tube technique using H-atom ARAS detection. The methods and the apparatus currently being used have been previously described [22,23] and only a brief description of the experiment will be presented here.

The shock-tube was constructed entirely from a 7-m (10.2 cm o.d.) 304 stainless steel tube with the cylindrical section being separated from the He driver chamber by a 4 mil unscored

1100-H18 aluminum diaphragm. The tube was routinely pumped between experiments to less than 1.3×10^{-11} bar by an Edwards Vacuum Products Model CR100P packaged pumping system. Shock-wave velocities were measured with eight equally spaced pressure transducers (PCB Piezotronics, Inc., Model 113A21) mounted along the downstream part of the test section and recorded with a 4094C Nicolet digital oscilloscope. Temperature and density in the reflected shock-wave regime were calculated from this velocity. This procedure has been given previously, and corrections for boundary layer perturbations have been applied [24–26]. The oscilloscope was triggered by pulses derived from the last velocity gauge signal. The photometer system was radially located at 6 cm from the endplate.

For H-atom detection, the lenses were crystalline MgF_2, and the resonance lamp beam intensity (filtered through 6 cm of dry air (21% O_2) to isolate the Lyman-α_H wavelength at 121.6 nm), was measured by an EMR G14 solar blind photomultiplier tube, as described previously [19,27–29], and was recorded with a LeCroy model LC334A oscilloscope. In order to measure the fraction of non-Lyman-α_H present in the resonance absorption emission lamp, an H_2 discharge flow system was used to create large [H] between the lamp and shock tube lens [30], thereby removing all of the Lyman-α_H lamp emission. The H-atom experiments were then performed with the discharge system turned off.

2.1. Gases

High purity He (99.995%), used as the driver gas, was from AGA Gases. Research grade Kr (99.999%), the diluent gas in reactant mixtures, was from Praxair, Inc. The $\sim$10 ppm impurities (N_2 < 5 ppm, O_2 < 2 ppm, Ar < 1 ppm, CO_2 < 0.5 ppm, H_2 < 1 ppm, H_2O < 3 ppm, Xe < 2 ppm, and THC < 0.2 ppm) are all either inert or in sufficiently low concentration so as to not perturb H-atom profiles. For H-atom detection, the microwave driven resonance lamp operated at 35 W and 1.4 Torr of ultra-high purity He (99.999%) (effective Doppler temperature, 470 K [30]). This grade of He contains a trace of hydrogenous impurities that is sufficient to give measurable Lyman-α_H radiation. CH_3OCH_3 (research grade, 99.9%) was obtained from Fluka and was further purified by bulb-to-bulb distillation, retaining only the middle third for mixture preparation. Gas mixtures were accurately prepared from pressure measurements using a Baratron capacitance manometer in an all glass high-purity vacuum line.

3. Theory

3.1. Electronic structure calculations

The $CH_3 + CH_3O$ interaction potential was characterized using the multireference CASPT2 method [31,32], a minimal active space of four electrons in three orbitals, and the aug-cc-pVDZ basis set. Two states were included in the CASSCF step of the CASPT2 calculation. At large fragment separations, the (4e,3o) active space corresponds to the radical orbital on the methyl fragment and the two p orbitals on the O atom of the methoxy fragment. Limited calculations were performed with the aug-cc-pVTZ basis set to examine the basis set convergence for key aspects of the interaction potential. The Molpro electronic structure package [33] was used.

The methoxy fragment was constrained to have C_{3v} symmetry, and both fragments were fixed at their isolated B3LYP/6-311++G** geometries when calculating the interaction potential. The symmetrized C_{3v} structure was chosen for the methoxy radical instead of the Jahn–Teller distorted C_s structure to simplify the potential energy surface fitting and the dynamics calculations.

In addition to the CASPT2 calculations described above on the $CH_3 + CH_3O$ interaction potential, we also report calculations on possible competing decomposition processes. In these calculations stationary point geometries were optimized at the CCSD(T)/aug-cc-pVDZ level followed by single point CCSD(T) calculations with aug-cc-pVTZ and aug-cc-pVQZ basis sets. The energies from the two single point calculations were then extrapolated to the complete basis set (CBS) limit.

3.2. Analytic six-dimensional surface

An analytic representation of the $CH_3 + CH_3O$ CASPT2(4e,3o)/aug-cc-pVDZ rigid fragment interaction potential energy surface (PES) was developed using a generalization of the recently described [34] rigid fragment interpolative moving least squares (IMLS) method [18]. The IMLS method was used here because it provides an automated strategy for converging the fitted surface to a specified accuracy with a minimal number of ab initio calculations. Briefly, an initial set of 2000 "seed" geometries was generated with coordinates distributed quasirandomly using a six dimensional Sobol sequence [35] evenly over the five orientation angles and with center of mass separations r_0 from 5 to 20 a_0 (1 $a_0 = 0.529$ Å). The distribution of center of mass separations was biased to favor small values of r_0 with the probability $p(r_0) = 0.953 \exp(-0.37(r_0/au - 5)) + 0.047$. Ab initio calculations of the energy and gradient using the CASPT2 method described above were carried out at the seed geometries. The resulting energies and gradients were used to obtain two initial IMLS fits: one "high order" fit and one "low order" fit. As discussed below, the order of the IMLS fit determines its flexibility. The high order fit is flexible enough to accurately describe the interaction potential. The low order fit is less flexible and is used to estimate the interpolation error of the high order fit. Specifically, the RMS and mean deviations in the two fits (evaluated at 40,000 randomly selected geometries) were evaluated; these deviations have been shown to be good indicators of the overall accuracy of the high order fit. The test points were again biased toward short values of r_0. The biased test set has larger estimated errors than unbiased test sets, but it yields a more useful probe of the chemically relevant regions.

The high order IMLS fit was systematically improved by generating additional ab initio energies and gradients at geometries identified as having the largest high order–low order differences. We note that by construction both high order and low order IMLS fits have essentially zero fitting error at the ab initio points included in the fits. The incorporation of new ab initio data into the fit produces new fits with essentially zero error at the new geometries as well. The new ab initio data were constrained to be no more than 15 kcal/mol above the separated fragments asymptote. Ab initio energies and gradients were calculated in parallel at these geometries (20 at a time) and added to the data set. New high and low order fits were generated using the augmented ab initio data set. This iterative process was repeated, systematically improving the quality of the fit until the RMS interpolation error was reduced below 0.3 kcal/mol. The final high order fit consists of 4366 ab initio energies and gradients and has RMS and mean interpolation errors of 0.28 and 0.13 kcal/mol, respectively. Note: the low order fit was used to estimate the interpolation errors and to identify the geometries at which new ab initio data were added to the set. The high order IMLS fit was used exclusively in the RDT dynamics calculations.

The symmetry of the CH_3 and CH_3O fragments was exploited in the IMLS fit as follows. The reference orientation for each fragment was chosen such that the threefold symmetry axes were aligned with the z-axis of the lab frame, thus permitting threefold mappings of the related Euler angles γ_1 and γ_2. In addition, after each ab initio calculation, a second symmetry-related data point was

obtained (at no cost) at the equivalent geometry obtained by flipping the methyl fragment so that the methoxy fragment is found on the opposite side of the plane of the methyl. Use of symmetry in this way improves overall fitting efficiency by a factor of 18.

The above has not described two critical features of any IMLS application: the basis set and the distance metric. The IMLS energy at any geometry $\vec{r}$ is evaluated as a weighted sum of local expansions V_j,

$$V(\vec{r}) = \sum_j w_j(\vec{r}) V_j(\vec{r}) \tag{E1}$$

centered at the geometries of the ab initio data. The basis function B_k defines the local expansion

$$V_j(\vec{r}) = c_{j,0} + \sum_k c_{j,k} B_k(\vec{r}) \tag{E2}$$

where $c_{j,k}$ are determined from weighted least squares fits to the full set of ab initio energies and gradients. The w_j can take many forms but must be steeply peaked so as to reproduce the ab initio energies and gradients. The form we use [18] is:

$$w_j(\vec{r}) = exp[-(d(\vec{r}_j, \vec{r})/D_j)^2]/((d(\vec{r}_j, \vec{r})/D_j)^6 + \varepsilon) \tag{E3}$$

where d is the distance metric, D_j is related to the density of ab initio points near $\vec{r}_j$, [18] and ε is a small number (10^{-14} in this case) to prevent singularities as d approaches 0.

The functional forms of the basis set and the coordinates in which they are expressed can significantly influence the accuracy of the fit relative to the number of ab initio data points in the fit. Here, the angular basis functions Ω were chosen to be products of rigid rotation functions,

$$\Omega_{L_1,L_2,K_1,K_2,M}(\gamma_1, \beta_1, \gamma_2, \beta_2, \alpha_1 - \alpha_2)$$
$$= R^{L_1}_{M,K_1}(0, \beta_1, \gamma_1) R^{L_2}_{-M,K_2}(\alpha_1 - \alpha_2, \beta_2, \gamma_2) \tag{E4}$$

where α_i, β_i, and γ_i are Euler angles for fragments i, $R^L_{M,K}$ are the real rotation matrices based on Wigner d-functions, [36] and the indices L_1, L_2, K_1, K_2, and M define the nodal structure of the basis function. The sum of L_1 and L_2 was limited to a maximum value of L_{max}, K_1 and K_2 may vary from $-L_1$ to L_1 and $-L_2$ to L_2, respectively, and M may vary from 0 to $\min(L_1, L_2)$. This choice for Ω is most appropriate at long-range, where the interaction potential is characterized by weak interactions. Although these angular basis functions are less suitable for short range geometries, the local expansions in the IMLS strategy allow for an accurate representation of the ab initio data over the entire range of geometries considered here.

The radial dependence of the basis functions was expressed as powers of the exponential of r_0 with a range parameter $a = 1$ Å^{-1}, such that

$$B_k(r_0, \gamma_1, \beta_1, \gamma_2, \beta_2, \alpha_1 - \alpha_2) = \exp(-ar_0)^N \Omega_{L_1,L_2,K_1,K_2,M} \tag{E5}$$

where $k = (N, L_1, L_2, K_1, K_2, M)$ is a composite basis function index. L_{max} and the maximum allowed value of N determine the order of the basis. For the higher order basis set, we choose $L_{max} = 3$ and $N = 1$–4, which results in 437 basis functions for each local expansion. For the lower order basis set, we choose $L_{max} = 2$ and $N = 1$–3, which results in 106 basis functions for each local expansion.

The geometry dependent weights w_j in Eq. (E1) are a function of the distance metric d that defines the effective "distance" between an evaluation geometry $\vec{r}$ and the geometries $\vec{r}_j$ of each of the ab initio data. In the present application,

$$d(\vec{r}_j, \vec{r})^2 \equiv \min_\Omega \sum_i |X_i(\vec{r}_j) - X_i(\vec{r})|^2 \tag{E6}$$

where X_i is the Cartesian vector of atom i and $\min_\Omega$ denotes minimization with respect to the relative rotation of the two geometries

about the axis connecting the centers of mass of the two fragments. This minimization is given by an analytic expression but in practice requires that all the ab initio points and each evaluation point be externally rotated so that the separation vector between the centers of mass of the two fragments are coincident with a common axis (say the z axis) whose origin is the center of mass of the total system. Permutation symmetry influences the value of d defined by Eq. (E6) because it changes the identity of the ith atom at the evaluation point relative to that at the ab initio point. As discussed above, there is an 18-fold permutation symmetry (relevant to rigid rotations) resulting in 18 different possible values of d, the minimum of which defines the final value of d used in w_j.

The use of gradient data, the specialized fitting basis, and the optimized and automated selection of ab initio information produced a great improvement in efficiency relative to the previous study of acetaldehyde [17]. The present IMLS fit required only 4366 ab initio energies and gradients, whereas in the acetaldehyde study a fit of permutationally invariant direct product multinomials in Morse variables required ~100,000 energies and considerable human effort in order to produce a fit of comparable quality.

3.3. One-dimensional corrections

One-dimensional corrections were developed to account for geometry relaxation, changes in the zero-point energy of the reactants, and limitations in the aug-cc-pVDZ basis set. Three approaches of the CH_3 and CH_3O fragments were considered: the minimum energy path for association (as), the minimum energy path for abstraction (ab), and a cut through the neighborhood of the roaming saddle point (sp). Along each approach, the CBS limit was estimated using the aug-cc-pVDZ and aug-cc-pVTZ basis sets and assuming l^{-3} scaling, where $l = 2$ and 3 for the aug-cc-pVDZ and aug-cc-pVTZ basis sets, respectively. The energetic effect and the change in the zero-point energy due to geometry relaxation were also calculated. To allow for fragment relaxation, these calculations were carried out for the A' state equilibrium geometry of Jahn–Teller distorted CH_3O. The CBS correction was found to be very similar for the C_s and C_{3v} CH_3O. For the abstraction correction, the geometry relaxation correction could not be reliably calculated for C–H distances shorter than 4 au, and the corrections along the abstraction approach were approximated at these distances.

The magnitudes of the individual and overall corrections are shown in Fig. 1. For the association channel in Fig. 1a, the magnitudes of the corrections are similar to those reported previously for CH_3 + HCO [17]. The well depth for the constrained-fragment abstraction is only 2.8 kcal/mol for CH_3 + CH_3O, as shown in Fig. 1b, and the geometry relaxation correction for this channel is greater than 10 kcal/mol at short distances. The geometry correction therefore qualitatively changes the shape of the potential energy surface for the CH_3 + CH_3O abstraction. For the CH_3 + HCO abstraction, on the other hand, the geometry correction was not greater than the depth of the constrained fragment well at relevant inter-fragment distances [17]. For the saddle point correction shown in Fig. 1c, the uncorrected energies and the individual corrections are of much smaller scale than those of the other two channels. The total correction is smaller than the other two channels and has a much weaker dependence on the fragment separation.

The one-dimensional corrections for the three approaches were combined into a global correction V_{cor} based on spline fits to the total corrections for each of the three approaches: V_{as}, which is a function of the C′–O distance (C′ labels the methyl carbon), V_{sp}, which is a function of the C′–Q distance (Q is the midpoint of C–O), and $\bar{V}_{ab}$, which is a weighted average of a spline fit V_{ab} to the total abstraction correction potential evaluated at each of the three C′–H distances
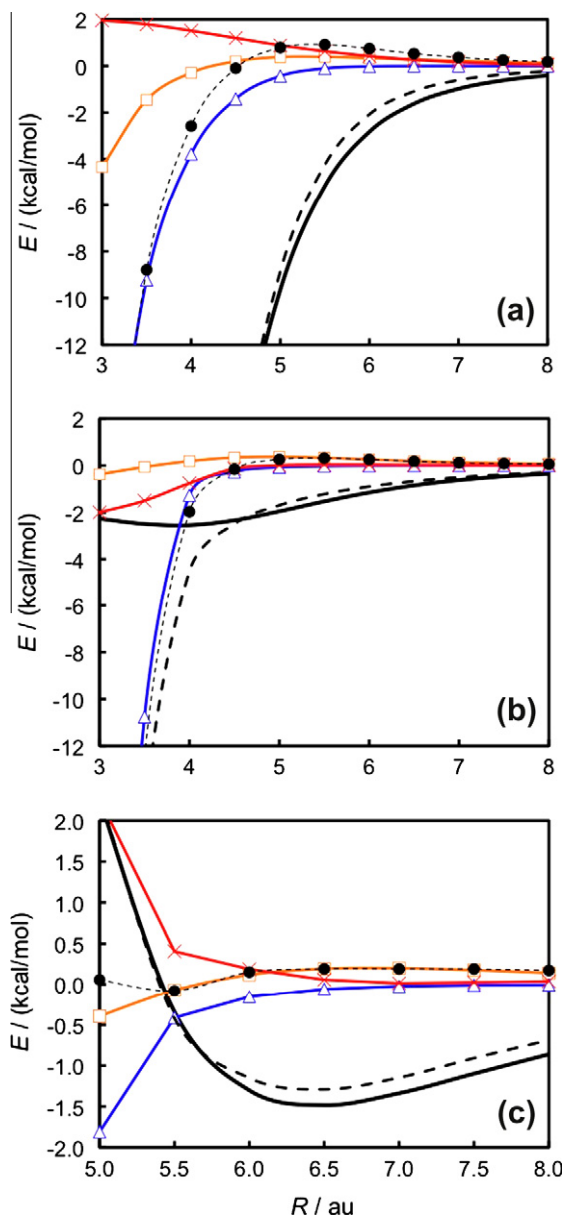
Fig. 1. One-dimensional correction potentials for the (a) association channel ($R = R_{C'O}$), (b) abstraction channel ($R = R_{C'H}$), and (c) saddle point region ($R = R_{C'Q}$), where Q is the midpoint of C–O in the methoxy fragment and C′ is the C atom in the CH$_3$ fragment. In each panel, (thick solid line) labels the uncorrected ab initio energies, (orange open squares, solid line) labels the difference between the CBS and uncorrected energies, (blue open triangles, solid line) labels the difference between the energies of the relaxed fragment geometries and uncorrected energies of the unrelaxed fragments, (red ×, solid line) labels the difference between the zero point energies of relaxed and unrelaxed fragments, (filled black circles, thin dotted line) labels the sum of the three previous difference energies, and (thick dashed black line) labels the corrected energies. (For interpretation of the references to color in this figure legend, the reader is referred to the web version of this article.)

$$\overline{V}_{ab} = \sum_i V_{ab}(R_{C'Hi})1/2(1 + \tanh((60° - \phi_i)/5°)), \qquad (E7)$$

where the hyperbolic tangent weights the contributions from the three C′–H distances as a function of the C′–C–H$_i$ angles ϕ_i. The total correction is given by

$$V_{cor} = V_{sp} + (V_{as} - V_{sp})F_1(s) + (\overline{V}_{ab} - V_{sp})F_2(s), \qquad (E8)$$

where F_x are hyperbolic tangent switching functions with range parameters of 5° and centers of 80° (F_1) or 100° (F_2), and s is a progress variable defined as the C′–Q–O angle.

A number of other simple strategies for combining the three one-dimensional corrections were also considered. These alternatives provided very similar results in the RDT calculations. A more detailed discussion of these higher level multichannel "one-dimensional" corrections will be presented in a future paper.

3.4. Trajectory calculations

The previous study on CH$_3$CHO [18] outlined an RDT approach for calculating the dissociative and roaming fluxes. This approach requires an appropriate PES in the reduced dimensions that describe transitional modes of motion along either the dissociation or roaming pathway. Using the CASPT2/aug-cc-pVDZ based IMLS fitted PES for the transitional mode motions in CH$_3$OCH$_3$, we have implemented that same procedure here. Briefly we calculated RDT dynamics on the corrected IMLS PES to estimate contributions to the reactive fluxes (reactive numbers of states) between the reactants and different products. This is accomplished by the propagation of rigid-body trajectories forward and backward on an appropriately weighted micro-canonical ensemble of configurations on a dividing surface separating reactants and different products. The rigid-body trajectories only explicitly involve the transitional degrees of freedom. The remaining conserved degrees of freedom are treated within a vibrationally adiabatic framework as part of the corrections to the PES described earlier. These corrections incorporate, as a function of the transitional degrees of freedom, the change in the vibrationally adiabatic zero-point energy from asymptotic values of the conserved modes. The trajectory results can be represented as micro-canonical statistical rates, trajectory-corrected for recrossing for both roaming and dissociation.

As discussed above, the trajectories are started on a dividing surface and used to correct the statistical flux for recrossing. In principle, any dividing surface that separates regions of phase space for the dissociative and the roaming process will do, although less optimal dividing surfaces lead to large amounts of recrossing and therefore large numbers of long-lived trajectories are required to converge the dissociative and roaming flux within small statistical uncertainties. The highly unsymmetrical dividing surfaces about the HCO fragment reported for CH$_3$CHO are not appropriate here for the highly symmetrical OCH$_3$ fragment. Multiple choices for the dividing surfaces were tested yielding comparable results (although in general requiring different numbers of trajectories). Most of the results used a sphere approximately centered on the C and another sphere approximately centered on the O in the OCH$_3$. A plane perpendicular to the C–O bond and intersecting the C–O bond near the center of mass of OCH$_3$ is then used to create two regions: a truncated sphere on the O side from which all dissociative and roaming processes start and a truncated sphere on the C side within which all roaming and abstraction processes end. The perpendicular plane nearly passes through the roaming saddle point. With this dividing surface, the RDT method required from 500 to 10,000 trajectories to converge the flux to typically a few percent for dominant processes. The flux of a less dominant process, which might be several orders of magnitude less than the flux of the dominant process, was converged within ∼10%.

The IMLS method [18] of fitting a PES results in global expansions of the PES about each ab initio point included in the fit. To evaluate the energy at a given point on the IMLS PES, the value of each expansion is assigned a weight [as in Eq. (E1)] that is a function of how near in the distance metric [Eq. (E6)] the ab initio point is to the given point. In the case of CH$_3$OCH$_3$, this approach would be unwieldy if all 437 basis functions expanded about each of 4366 ab initio points had to be evaluated to determine an energy on the IMLS PES. Instead, a neighbor-list scheme was used in which a ranked list of nearby ab initio points was established with the

evaluations terminated when the weight of the last point is some input cutoff fraction of the accumulated sum. The weighted summation of the value of the global expansion of each ab initio point on the list gives the IMLS energy. As will be discussed in a later paper, there are approximations to the ranked list that avoid calculating the full distance metric for each of 4366 ab initio points for every IMLS evaluation. Aggressive application of these approximations and the cutoff fraction can speed up the average IMLS evaluation time in trajectory studies by more than an order of magnitude, but at the price of an increased drift in the energy conservation of the trajectory. Convergence tests of RDT flux established the values of the cutoff fraction and parameters controlling approximations to the ranked list. The resulting rms error in trajectory energy conservation for any trajectory run was always below 0.02 kcal/mol. The flux determined from these trajectory runs was within the statistical error bars of flux calculated from faster, preliminary trajectory runs with an order of magnitude larger rms error. If run on a single processor, the resulting RDT trajectory calculations took between a day and a week depending on the energy (low energy trajectories take much longer). Production level trajectory runs were generally done on eight processors at a time to shorten turnaround to no more than a few days.

3.5. Kinetics calculations

The pressure dependence of the experiments is represented with one-dimensional master equation calculations [37] in energy employing an exponential down collisional energy transfer model and Lennard–Jones collision frequencies. The average downward energy transfer is taken to be $100(T/300)^{0.85}$ cm^{-1}. This expression employs a standard temperature dependence [38] and is normalized to yield rate coefficients that are in good agreement with the experimental measurements of the overall decomposition rate.

The reactive fluxes for channels (R1) and (R2) are obtained from the trajectory calculations with the IMLS fitted ab initio potential energy surface. The final results include the correction, V_{cor}. The reactive fluxes for the channels with well-defined saddle points are obtained from tunneling corrected conventional transition state theory employing rigid rotor harmonic oscillator assumptions for the energy levels. The two methyl rotors in DME are treated as separable one-dimensional hindered rotors, while the remaining vibrational modes were treated as harmonic oscillators. The CCSD(T)/aug-cc-pVDZ calculated rovibrational properties were employed in these flux analyses.

4. Results and discussion

4.1. Experimental results

4.1.1. High temperature/dilute experiments

Two sets of experiments were performed in the present work. The first set utilized very dilute mixtures (<1 ppm) of CH$_3$OCH$_3$ thereby suppressing secondary reactions that deplete [H]. This suppression allowed direct measurements of the branching ratios to the C–O bond fission channel through (R1). In these experiments, H-atoms were measured from the subsequent instantaneous CH$_3$O-radical decomposition from (R1) to give H + CH$_2$O. Fifty experiments were performed that span a temperature range, 1406–1764 K, and pressure range, 0.20–1.25 atm. Figure 2 shows a typical H-atom profile at T = 1572 K using [CH$_3$OCH$_3$]$_0$ = 1.15 × 10^{12} molecules cm^{-3}, yielding [H]$_\infty$ = 9.05 × 10^{11} atoms cm^{-3}. The simulated results using the mechanism given in Table 1 are shown as the solid black line. The long dashed lines show variations in the overall decomposition rate constant, k_{total}, by ±40%, and the dotted lines show variations of ±0.1 in the branching ratio giving H-atoms, BR$_1$ = k_1/k_{total}. The simulations were performed using the SENKIN [39] suite of
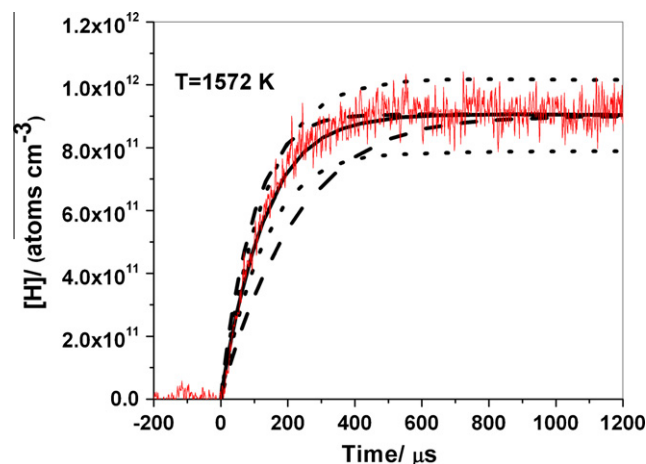

Fig. 2. [H] profile at 1572 K. The solid line is a fit over the entire time range using the mechanism in Table 1 with $k_1 + k_2$ = 8000/s and BR$_1$ = 0.79. The dashed lines represent changes in $k_1 + k_2$ by ±40% with BR$_1$ = 0.79. The dotted lines represent changes in BR$_1$ by ±0.1 with $k_1 + k_2$ fixed at 8000 s^{-1}. The conditions for the experiment at T_5 = 1572 K are P_1 = 10.95 Torr, M_s = 2.506, ρ_5 = 2.103 × 10^{18} molecules cm^{-3}, [CH$_3$OCH$_3$]$_0$ = 1.15 × 10^{12} molecules cm^{-3}.

programs in the CHEMKIN package. An example sensitivity plot is shown in Fig. 3 for Fig. 2 experiment where it is seen that the profile depends only on k_1 and k_2; i.e., secondary reactions involving H are completely unimportant since the maximum value of [H] is so low, indicating that first-order analysis is appropriate. The normalized sensitivity coefficients are defined as $\partial \ln[H]/\partial \ln k_i$ where [H] is the H-atom concentration and k_i the rate constant for reaction i. Hence, the present results are a direct measure of dissociation.

First-order analysis gives the simple closed form result

$$[H]_t = \{k_1[CH_3OCH_3]_0/(k_1 + k_2)\} \times \{1 - \exp(-(k_1 + k_2)t)\}, \quad (E9)$$

where [H]$_\infty$ = k_1[CH$_3$OCH$_3$]$_0/(k_1 + k_2)$ and BR$_1$ = $k_1/(k_1 + k_2)$. For the data shown in Fig. 2, inspection shows that BR$_1$ = 9.05 × 10^{11}/1.15 × 10^{12} = 0.79. We have determined the total decomposition rate constant, $k_t = k_1 + k_2$, from temporal profiles like that shown in Fig. 2 using Eq. (E9) by adjusting k_t and BR$_1$ to obtain a good fit to the experimental profile. Subsequently, we determine k_1 and k_2 from the measured BR$_1$ for the same experiment. The results are given in Table 2 along with the inferred BR$_2$ (=1 − BR$_1$). Using these first order analyses for k_1 and k_2 in Table 1 mechanism to simulate the profiles, the same results are recovered as those using Eq. (E9). This confirms the observations from the sensitivity analysis of Fig. 3 that first-order analysis is appropriate for all the experiments reported in Table 2.

The decomposition rate constants at various densities are shown in Figs. 4 and 5 as Arrhenius plots. The major decomposition pathway is reaction (R1), as assumed in all previous work. However, we find significance to reaction (R2) that is entirely due to the roaming mechanism. As discussed in the theory results below, all other channels are kinetically insignificant contributors for the conditions of the present experiments. The temperature and density dependences of BR$_2$ are shown in Fig. 6. A comparison of the highest and lowest density data shows that BR$_2$ tends to vary with ρ. Also, it appears that BR$_2$ tends to decrease with increasing temperature. Overall, for the full temperature and pressure range of the experiments, the mean value for BR$_2$ is 0.19 ± 0.07. The value of BR$_2$ and its T and ρ dependence will be addressed theoretically in Section 4.2.

4.1.2. Low temperature/more concentrated experiments

The second set of experiments used more concentrated mixtures (5–10 ppm) that are similar to those from the recent H-ARAS

Table 1
Mechanism for CH_3OCH_3 Decomposition and $H + CH_3OCH_3$.[a]

1	$CH_3OCH_3 \rightarrow CH_2O + H + CH_3$	k_1 = to be fitted	[Present]
2	$CH_3OCH_3 \rightarrow CH_4 + CH_2O$	k_2 = to be fitted	[Present]
3	$H + CH_3OCH_3 \rightarrow CH_3OCH_2 + H_2$	k_3 = to be fitted	[Present]
4	$CH_3OCH_2 \rightarrow CH_3 + CH_2O$	$k_4 = 4.45 \times 10^{14}T^{-0.22} \exp(-13,702\ \text{K}/T)$	[46]
5	$CH_2O + Kr \rightarrow HCO + H + Kr$	$k_5 = 1.019 \times 10^{-8} \exp(-38,706\ \text{K}/T)$	[20]
6	$CH_2O + Kr \rightarrow H_2 + CO + Kr$	$k_6 = 4.658 \times 10^{-9} \exp(-32,110\ \text{K}/T)$	[20]
7	$HCO + Kr \rightarrow H + CO + Kr$	$k_7 = 6.00 \times 10^{-11} \exp(-7722\ \text{K}/T)$	[47]
8	$CH_3 + CH_3 \rightarrow C_2H_6$	$k_8 = f(\rho, T)$	[48]
9	$CH_3 + CH_3 \rightarrow C_2H_4 + 2H$	$k_9 = 5.26 \times 10^{-11} \exp(-7392\ \text{K}/T)$	[28]
10	$CH_3 + CH_3OCH_3 \rightarrow CH_4 + CH_3OCH_2$	$k_{10} = 4.45 \times 10^{-23}T^{3.78} \exp(-4847\ \text{K}/T)$	[3]

[a] All unimolecular rate constants are in s^{-1} and bimolecular rate constants are in cm^3 molecule^{-1} s^{-1}.
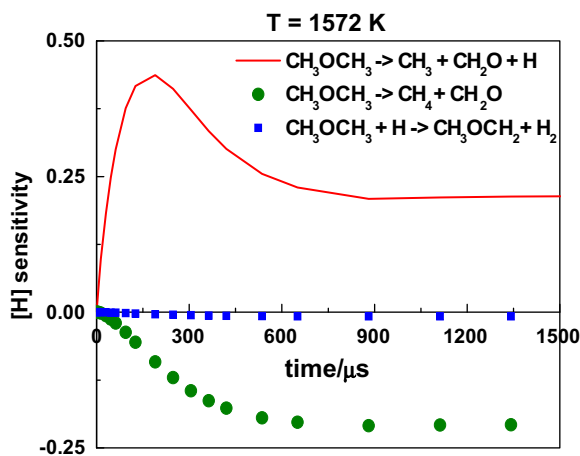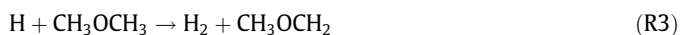

Fig. 3. H-atom sensitivity analysis for the 1572 K profile shown in Fig. 2 using the full reaction mechanism scheme. The three most sensitive reactions are shown in the inset.

study of Fernandes et al. [9]. Under these conditions, secondary reactions begin to perturb the [H] profile, particularly the abstraction reaction,

$$H + CH_3OCH_3 \rightarrow H_2 + CH_3OCH_2 \qquad (R3)$$

Hence, the H-atom yields at long times are suppressed. Consequently, these experiments permitted simultaneous measurements for (R1) and (R3) to be made. Seventeen experiments were performed spanning a temperature range, 1149–1465 K. Figure 7 shows a typical H-atom profile from an experiment at 1248 K using $[CH_3OCH_3]_0 = 5.38 \times 10^{13}$ molecules cm^{-3}. The corresponding sensitivity analysis, Fig. 8, clearly shows that the two reactions that determine the profile in Fig. 7 are indeed only R1 and R3. There is little or no sensitivity to R2. Initial values of k_1 for simulating the profile in Fig. 7 are obtained by extrapolation of the results in Table 2 to lower temperatures by means of an Arrhenius expression for each particular reflected shock density range. Initial values of k_3 are taken from the work of Takahashi et al. [21]. The black solid line is a fit to the profile in Fig. 7 using the mechanism in Table 1 with final optimized values of k_1 (that matches the early rise time) and k_3 (that provides a best fit to the late time). The dashed lines are changes to k_3 by ±50% and these significantly degrade the fit to the profile in comparison to the optimized value from modeling. The experimental conditions as well as the optimized k_1 and k_3 values obtained from the simulations are summarized in Table 3. With these experimental results, the rate constant database for (R1) now spans the temperature range from 1149 to 1764 K.

The abstraction rate constants for (R3) over the temperature range 1149–1465 K in Table 3 can be represented by an Arrhenius expression in units, cm^3 molecule^{-1} s^{-1},

$$k_3 = 2.147 \times 10^{-9} \exp(-5914/T) \qquad (E10)$$

At the one standard deviation level, the present experiments are within ±31% of the line determined from Eq. (E10). Combining the present data (Table 3) for reaction (R3) with the data of Takahashi et al. [21] and the lower-T results of Tranter and Walker [40], Faubel et al. [41], Lee et al. [42], and Meagher et al. [43], rate constants have been evaluated over the temperature range, 273–1465 K, to give

$$k_3 = 6.54 \times 10^{-24}T^{4.13} \exp(-896/T)\ \text{cm}^3\ \text{molecule}^{-1}\ \text{s}^{-1} \qquad (E11)$$

This evaluation, Eq. (E11), is within ±9% of the Arrhenius expression derived from the present data, Eq. (E10), over the temperature range of overlap. A plot of Eq. (E11) and the data from which it was derived is shown in Fig. 9. We have chosen to use the lower-T data of Meagher et al. [43] and Faubel et al. [41] for the evaluation despite the uncertainties in these measurements (due to stoichiometric corrections employed to obtain rate constants). It is evident that the room-T measurements of Slemr and Warneck [44] must be in error [42] and consequently they were ignored in the present evaluation. The data of Fernandes et al. [9] was also not included in this evaluation since they assumed a T-independent value for k_3 in order to extract k_1 values.

The theoretical predictions of Takahashi et al. [21] appear to be in better agreement with the lower-T measurements of Meagher et al. [43] than the more direct resonance-fluorescence measurements of Lee et al. [42]. The more rigorous QCISD(T)/6-311 + G(3df,3pd)// MP2/6-311 + G(d,p) based variational TST based theoretical predictions of Wu et al. [45] are in reasonable agreement with the low-T data, but systematically overpredict the abstraction rate constants for (R3) by a factor of 2–3 at high-T (>500 K).

4.2. Theoretical results

4.2.1. $CH_3 + CH_3O$ interaction potential

Contour diagrams illustrating the interaction of a rigid CH_3 radical with a rigid CH_3O radical are provided in Fig. 10. The strongly attractive contours in the lower left and right portions of the plots illustrate the barrierless addition of the methyl radical to the O atom of methoxy from either the cis or trans sides of the in-plane H-atom. This addition is barrierless for the full range of torsion angles. The attractive contours toward the upper left of the plots illustrate the barrierless approach of the methyl radical toward the H-atom in methoxy that is in the plane of the plot. Similar barrierless paths exist for approach to the two out-of-plane H-atoms. The $CH_3 + CH_3O$ abstraction reaction requires significant relaxation of the rigid fragment structures. As a result, the minimum potential for the rigid approach to the H-atom is only about 3 kcal/mol (cf. Fig. 10). Inclusion of the relaxation correction dramatically changes the interaction potential in the abstraction region, as illustrated in Fig. 11.

The estimated RMS and mean errors for the IMLS fit to the potential (0.28 and 0.13 kcal/mol, respectively) provide measures of the accuracy of the fit. However, it is not clear to what extent these

Table 2
Higher-T rate data: $CH_3OCH_3 \rightarrow CH_3 + H + CH_2O$ and $CH_3OCH_3 \rightarrow CH_4 + CH_2O$.

P_1[a] (Torr)	M_s[b]	ρ_5 (10^{18} cm^{-3})[c]	T_5 (K)[c]	P_5 (Torr)[c]	k_1[d]	k_2[d]	BR_2[e]
$X_{CH3OCH3} = 1.111 \times 10^{-6}$							
5.94	2.580	1.173	1659	201.6	8910	2090	0.19
5.92	2.549	1.156	1622	194.2	8200	1800	0.18
5.92	2.502	1.135	1568	184.3	3666	1034	0.22
5.89	2.495	1.126	1560	181.9	3080	920	0.23
5.86	2.357	1.056	1406	153.8	547.5	202.5	0.27
5.91	2.407	1.090	1461	165.0	1184	416	0.26
5.95	2.438	1.112	1495	172.2	1848	552	0.23
5.91	2.650	1.196	1743	215.9	15,840	2160	0.12
5.92	2.561	1.161	1636	196.7	8610	1890	0.18
5.93	2.616	1.186	1701	209.0	12,600	2400	0.16
$X_{CH3OCH3} = 5.469 \times 10^{-7}$							
10.91	2.459	2.056	1519	323.5	2464	736	0.23
10.95	2.470	2.073	1531	328.7	2470	780	0.24
10.92	2.438	2.040	1495	315.9	1312.5	437.5	0.25
10.87	2.452	2.043	1511	319.8	2926	874	0.23
10.91	2.520	2.107	1589	346.8	5197.5	1552.5	0.23
10.79	2.593	2.141	1674	371.2	13,280	2720	0.17
10.88	2.578	2.147	1657	368.5	8910	2090	0.19
10.87	2.523	2.101	1592	346.5	6560	1440	0.18
10.95	2.459	2.064	1519	324.7	2618	782	0.23
10.95	2.506	2.103	1572	342.4	6320	1680	0.21
$X_{CH3OCH3} = 1.111 \times 10^{-6}$							
10.93	2.668	2.225	1764	406.5	19,350	3150	0.14
10.84	2.598	2.154	1680	374.8	14,580	3420	0.19
10.92	2.608	2.178	1692	381.7	14,000	3500	0.20
10.95	2.519	2.113	1587	347.3	5304	1496	0.22
10.89	2.442	2.038	1500	316.6	2485	1015	0.29
$X_{CH3OCH3} = 5.469 \times 10^{-7}$							
15.91	2.406	2.927	1458	442.0	1005	495	0.33
15.90	2.552	3.090	1620	518.5	9000	3000	0.25
15.84	2.545	3.071	1612	512.8	8625	2875	0.25
15.75	2.507	3.012	1567	488.9	5810	1190	0.17
15.88	2.494	3.023	1554	486.6	2736	1064	0.28
15.85	2.419	2.931	1472	446.9	1190	560	0.32
15.94	2.455	2.990	1512	468.3	1988	812	0.29
15.82	2.538	3.060	1604	508.4	9960	2040	0.17
15.98	2.499	3.047	1560	492.4	4140	1610	0.28
$X_{CH3OCH3} = 2.628 \times 10^{-7}$							
15.97	2.521	3.070	1585	504.0	8280	720	0.08
15.86	2.453	2.973	1509	464.7	2795	455	0.14
15.89	2.385	2.898	1436	431.1	810	190	0.19
$X_{CH3OCH3} = 4.351 \times 10^{-7}$							
15.94	2.547	3.093	1614	517.1	7920	1080	0.12
15.78	2.469	2.975	1526	470.2	3120	880	0.22
15.72	2.546	3.049	1613	509.4	8602.5	647.5	0.07
15.89	2.563	3.100	1633	524.4	10,005	1495	0.13
15.88	2.421	2.939	1475	449.0	1760	440	0.20
$X_{CH3OCH3} = 2.628 \times 10^{-7}$							
30.72	2.435	5.604	1470	853.3	2400	600	0.20
30.70	2.543	5.836	1589	960.5	19,200	800	0.04
30.93	2.390	5.537	1421	815.0	1496	204	0.12
30.64	2.500	5.733	1541	915.1	4895	605	0.11
30.71	2.517	5.782	1560	934.3	9300	700	0.07
30.59	2.437	5.585	1472	851.5	2666	434	0.14
30.87	2.447	5.628	1482	863.9	2580	420	0.14
30.47	2.415	5.513	1448	826.9	1344	256	0.16

[a] The initial pressure.
[b] The error in measuring the Mach number, M_s, is typically 0.5–1.0% at the one standard deviation level.
[c] Quantities with the subscript 5 refer to the thermodynamic state of the gas in the reflected shock region.
[d] Rate constants: first order in s^{-1}.
[e] $BR_2 = k_2/(k_1 + k_2)$.

statistical errors affect the predicted kinetics. The *relative* error in the interaction energy in the transition state region of the potential is often a good measure of the relative error in the predicted kinetics. We have found in previous numerical simulations that, at least for modest errors, a given percent error in the minimum energy path potential roughly correlates with a corresponding percent error in the predicted rate coefficient.

One can obtain some sense of the relative errors via visual comparisons. Thus, we have presented a contour plot in Fig. 10b of a direct spline fit to a 100×100 grid of ab initio data. The strong similarity of the plots in Fig. 10a and b provides confidence in the IMLS fit. There are some visible discrepancies, particularly in the abstraction region of the potential, where the IMLS fit is too attractive. However, the error in that particular region is
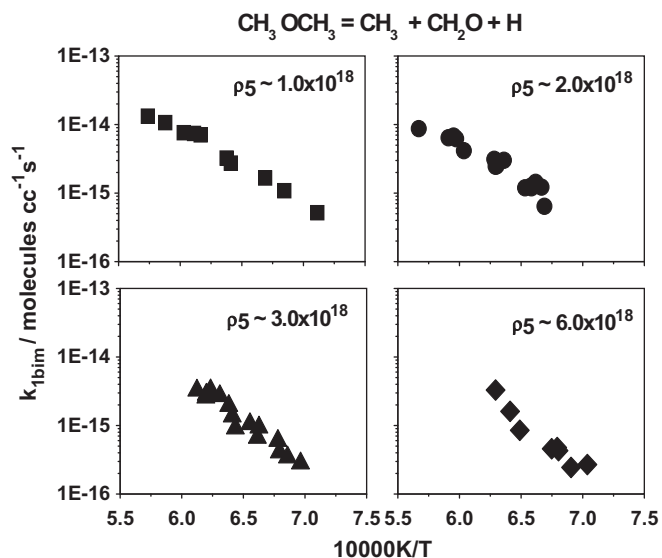
Fig. 4. Experimental bimolecular rate constants for $CH_3OCH_3 + Kr \rightarrow CH_3 + H + CH_2O + Kr$. The four panels represent data obtained at four different reflected shock densities from $(1–6) \times 10^{18}$ molecules cm^{-3}.
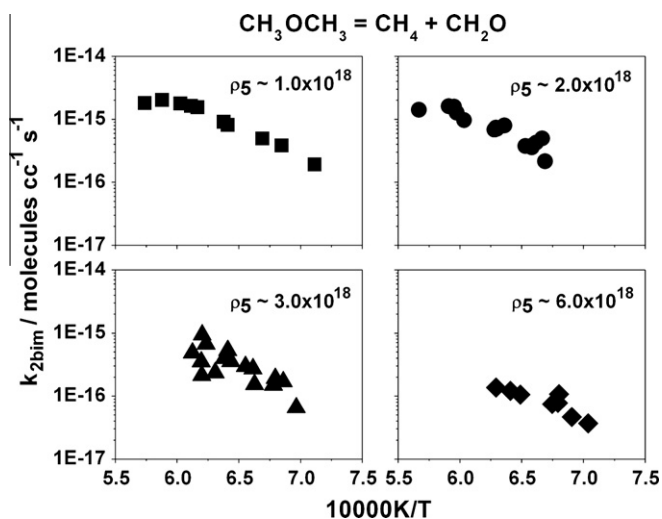

Fig. 6. Experimental branching ratios for reaction (R2) in the thermal decomposition of CH_3OCH_3. The four panels represent data obtained at four different reflected shock densities from $(1–6) \times 10^{18}$ molecules cm^{-3}.

Fig. 5. Experimental bimolecular rate constants for $CH_3OCH_3 + Kr \rightarrow CH_4 + CH_2O + Kr$. The four panels represent data obtained at four different reflected shock densities from $(1–6) \times 10^{18}$ molecules cm^{-3}.

Fig. 7. [H] profile at 1248 K. The solid line is a fit over the entire time range using the mechanism in Table 1 with the fitted values for k_1 and k_3 given in Table 3. The dashed lines represent changes in k_3 by ±50%. The conditions for the experiment at T_5 = 1248 K are P_1 = 30.64 Torr, M_s = 2.222, ρ_5 = 5.074 × 10^{18} molecules cm^{-3} and $[CH_3OCH_3]_0$ = 5.382 × 10^{13} molecules cm^{-3}.

ameliorated by the large 1D attractive correction that is applied (see Section 3.3) to that region (Fig. 11). The plots in Fig. 12, which illustrate the uncorrected IMLS fitted and directly calculated minimum energy pathway energies for both the addition and abstraction reactions, provide a quantitative indication of these discrepancies. The IMLS fit for the addition path is very accurate, but is in error by as much as 30% for the abstraction path.

On the corrected PES, the relative IMLS error along the abstraction reaction path is much smaller because of the size of the correction (see Fig. 11). However, where this IMLS error is largest in Fig. 12 is at C′–H distances near 4 a_0 where, as discussed previously, the correction itself is hard to accurately determine. Furthermore, the interpolation used in the correction is also not perfect as can be seen in Fig. 11 in the 1 kcal/mol dimple in the PES for approaching the C end of methoxy along its C–O axis. A nearly identical dimple is found when the correction is added to the
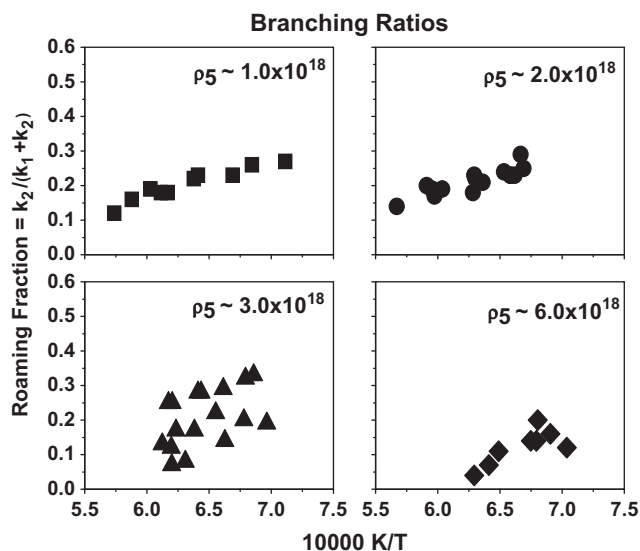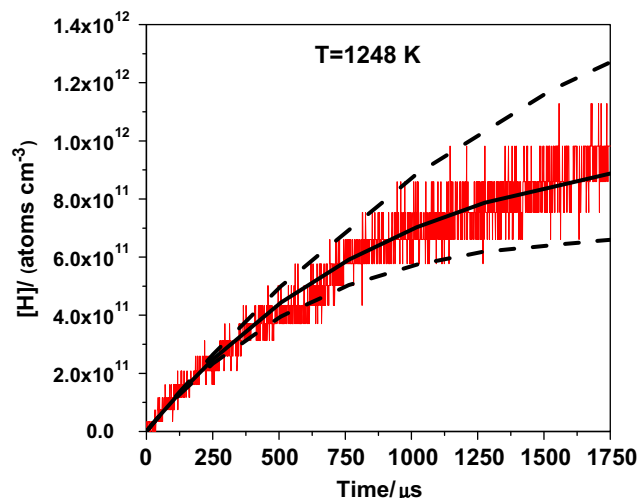
spline fit of ab initio results in Fig. 10b. Since there is no trace of this feature in either uncorrected potential in Fig. 10, this is most likely a modest interpolation deficiency in the 1-D correction.

A final test of the IMLS fitting is provided by a comparison of VRC-TST predictions for the high pressure kinetics employing either directly determined ab initio energies or the IMLS fit. Such VRC-TST predictions for the $CH_3 + CH_3O$ addition and abstraction rate constants are plotted in Fig. 13. The two predictions for the addition rate coefficient are in remarkably good agreement, differing by only a few percent at most. These very modest deviations are largest at high temperature because at high energy the transition state moves in to slightly less than 5 bohr, while the IMLS surface is restricted to separations of 5 bohr and greater. The deviations for the abstraction channel are somewhat greater, with the IMLS fit based results being as much as 1.28 times greater than
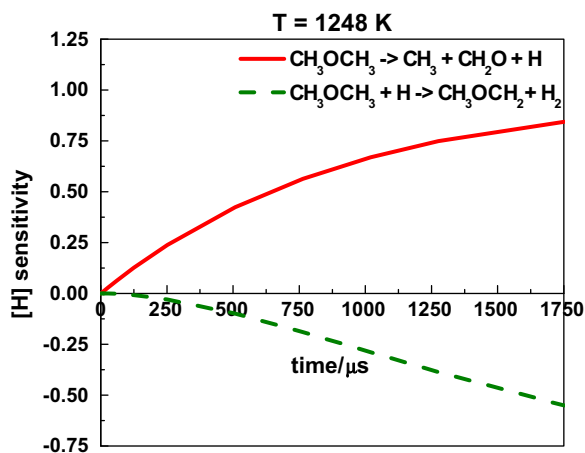
Fig. 8. H-atom sensitivity analysis for the 1248 K profile shown in Fig. 7 using the full reaction mechanism scheme in Table 1. The two most sensitive reactions are shown in the inset.

Table 3
Lower-T rate data: $CH_3OCH_3 \rightarrow CH_3 + H + CH_2O$, $H + CH_3OCH_3 \rightarrow H_2 + CH_3OCH_2$.

P_1^a (Torr)	M_s^b	ρ_5 (10^{18} cm^{-3})^c	T_5 (K)^c	P_5 (Torr)^c	k_1^d	k_3^e
$X_{CH3OCH3} = 5.259 \times 10^{-6}$						
10.96	2.257	1.883	1299	253.3	70	2.00(−11)
10.93	2.387	1.998	1439	297.7	750	3.50(−11)
10.92	2.254	1.874	1297	251.7	85	1.90(−11)
10.92	2.287	1.905	1332	262.8	130	2.25(−11)
10.91	2.416	2.026	1465	307.4	1300	5.00(−11)
10.82	2.201	1.806	1242	232.3	33	1.70(−11)
10.92	2.315	1.931	1361	272.2	280	3.00(−11)
10.87	2.338	1.943	1386	278.9	500	3.50(−11)
$X_{CH3OCH3} = 5.259 \times 10^{-6}$						
15.91	2.284	2.776	1330	382.3	80	2.75(−11)
$X_{CH3OCH3} = 1.061 \times 10^{-5}$						
15.95	2.277	2.774	1323	380.1	80	2.00(−11)
15.87	2.198	2.655	1242	341.5	17	1.70(−11)
15.83	2.273	2.748	1318	375.1	70	2.00(−11)
15.95	2.228	2.709	1273	357.1	26	1.90(−11)
$X_{CH3OCH3} = 1.061 \times 10^{-5}$						
30.64	2.222	5.074	1248	655.8	21	2.00(−11)
30.87	2.225	5.120	1251	663.3	20	2.00(−11)
30.80	2.121	4.830	1149	574.7	2	1.50(−11)
30.68	2.150	4.890	1177	596.0	4	1.66(−11)

^{a} The initial pressure.
^{b} The error in measuring the Mach number, M_s, is typically 0.5–1.0% at the one standard deviation level.
^{c} Quantities with the subscript 5 refer to the thermodynamic state of the gas in the reflected shock region.
^{d} Rate constants: first order in s^{-1}.
^{e} Rate constants: bimolecular in cm^3 molecule^{-1} s^{-1}.

the direct ab initio based results. This modest overestimate of the abstraction rate coefficient is directly related to the overestimate of the attractiveness of the abstraction pathway.

The above predictions for the addition and abstraction rate coefficients include the "one-dimensional" correction to either the IMLS potential or the directly calculated rigid fragment ab initio energies. Beyond any imperfections in the correction, we have not considered the effect of either Jahn–Teller or spin–orbit splittings on the reactant partition functions. Thus, these predictions may be in considerable error in an absolute sense. Unfortunately, there do not appear to be any reliable experimental measurements of these rate coefficients. The consideration of such Jahn–Teller and spin–orbit splittings was deemed beyond the scope of the present analysis, particularly since their effect on
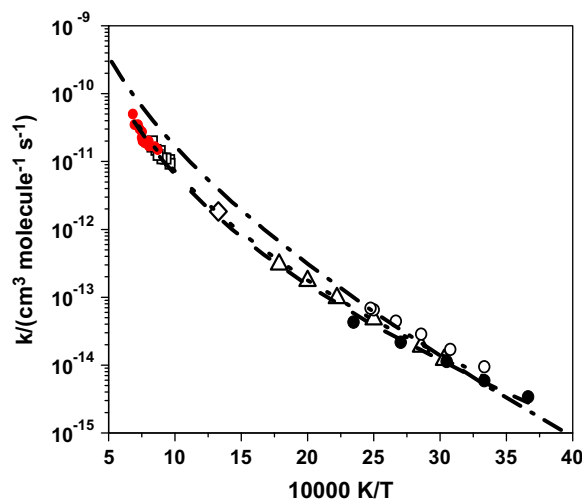

Fig. 9. Arrhenius plot of the $H + CH_3OCH_3$ rate constants. (- - -) – three parameter evaluation, present work, Eq. (E11), (273–1465 K), (…) – Theory, Takahashi et al. [21], (298–1500 K), (-.-) – Wu et al. [45], (250–2000 K), (◇) – Tranter and Walker [40] (753 K), (○) – Meagher et al. [43] (300–404 K), (△) – Faubel et al. [41], (330–560 K), (□) – Takahashi et al. [21], (1038–1208 K), (●) – Lee et al. [42], (273–426 K), (● red) – present work, large concentration CH_3OCH_3 mixtures (Table 3), (1149–1465 K).

the transition state partition functions will be greatly reduced. Correspondingly, their neglect should be ameliorated in our present overall focus on the dissociation rather than association process.

4.2.2. Roaming pathway

The structure of the saddle point for the roaming-radical pathway is shown in Fig. 14. The structure is of C_s symmetry having a CO distance for the breaking C–O bond of 3.3 Å and a CH distance for the new C–H bond of 2.5 Å. For reference, this saddle point correlates with coordinates of ∼ (−6, −1) in the contour plots of Fig. 10 and 11. The CASPT2 calculations predict this saddle point to lie 1.6 kcal/mol below the $CH_3O + CH_3$ asymptote. For comparison, the uncorrected and corrected IMLS fits yield energies of 1.8 and 1.5 kcal/mol, respectively, at the CASPT2 saddle point geometry.

An unusual feature of this reaction path is that the roaming methyl radical inverts, i.e., the face of the methyl that starts off bonded to the oxygen is not the same face that ends up bonded to the hydrogen. This inversion can be seen clearly in an animation of the IRC available as a web enhanced object (see Supplemental material). This inversion of a roaming methyl radical has been observed before in the decomposition of alkanes and has been explained using Orbital Phase Continuity Principle (OPCP) arguments [11].

4.2.3. Competing pathways

Four possible competing decomposition pathways were examined. These were as follows:

$$CH_3OCH_3 \rightarrow H + CH_3OCH_2 \tag{R4}$$
$$\rightarrow CH_3OH \cdots {}^1CH_2 \rightarrow CH_3OH + {}^1CH_2 \tag{R5}$$
$$\rightarrow CH_3OCH + H_2 \tag{R6}$$
$$\rightarrow CH_2O + CH_4 \tag{R7}$$

where (R7) refers to the possibility of a competing tight transition state to the roaming products. The results of the CCSD(T)/CBS// CCSD(T)/aug-cc-pVDZ calculations are summarized in Table 4 and Fig. 15. Reaction (R7) is nominally Woodward–Hoffman forbidden. All attempts to find a tight transition state for (R7) failed. The high pressure rate constants for dissociation to channels (R4), (R5), (R6)
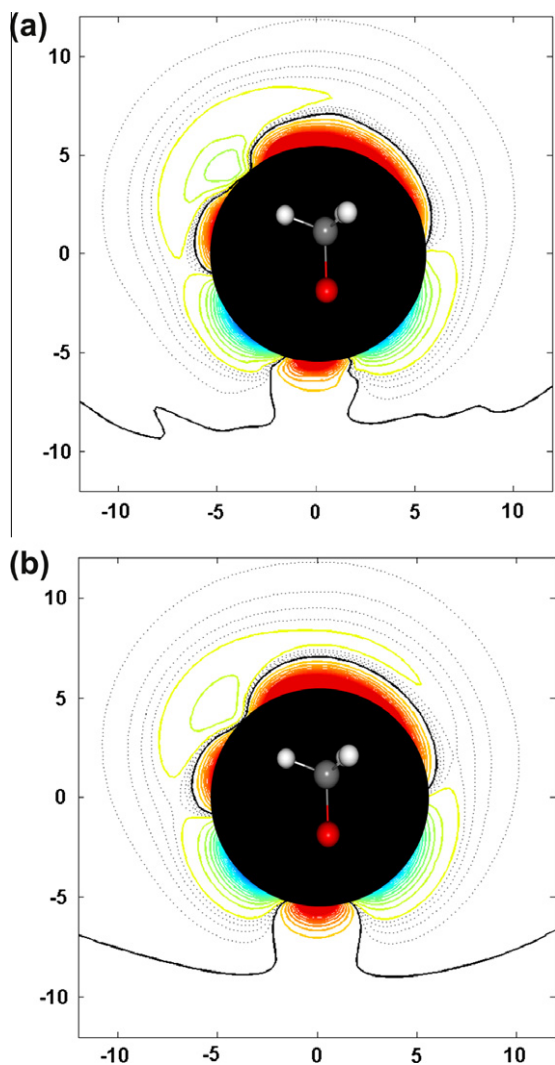
(a)

(b)

Fig. 10. Contour plots of the $CH_3O + CH_3$ interaction potential. Plot (a) is of the automatically generated IMLS PES fit to the CASPT2/aug-cc-pVDZ data. Plot (b) is a two-dimensional spline fit directly to a 100×100 grid of ab initio data points. Contours are: color (1 kcal/mol spacing), dashed ($-0.2, -0.4, \ldots, -0.8$), solid (0.0). Increasingly blue contours are attractive, while increasingly red are repulsive. (For interpretation of the references to color in this figure legend, the reader is referred to the web version of this article.)

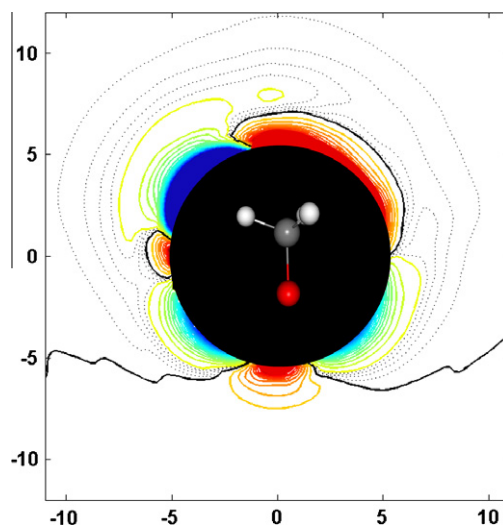**Fig. 11.** Contour plot of the $CH_3O + CH_3$ interaction potential from the IMLS fit including the 1D potential corrections (with the same contours as Fig. 10). (For interpretation of the references to color in this figure legend, the reader is referred to the web version of this article.)
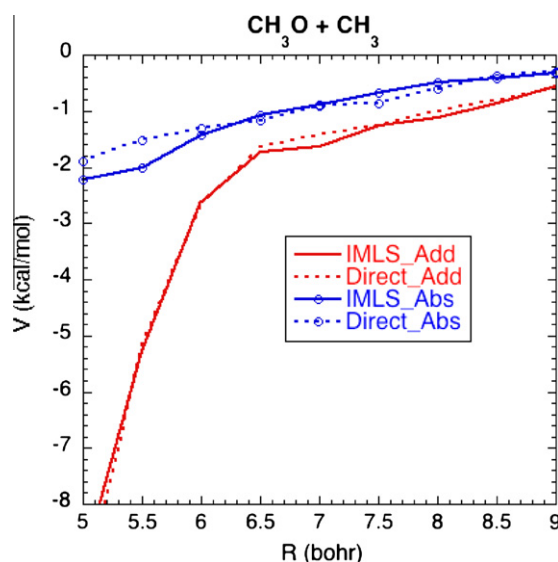

Fig. 12. Plots of IMLS fit and ab initio data along the addition (red lines) and abstraction (blue lines with open circles) reaction paths. The solid and dashed lines denote the IMLS fit and ab initio data, respectively. For the addition R denotes the C′O distance, while for the abstraction it denotes the C′H distance. (For interpretation of the references to color in this figure legend, the reader is referred to the web version of this article.)

were evaluated with transition state theory and compared with the calculated high pressure rate constant for the dissociation to $CH_3 + CH_3O$ (R1).

Reaction (R4) is predicted to be 12 kcal/mol higher than the $CH_3O + CH_3$ asymptote, comparable to the difference found [17] in CH_3CHO for the analogous channel to form $H + CH_2CHO$. Presuming a typical reverse recombination rate constant of 4×10^{-10} cm^3 molecule^{-1} s^{-1} for this channel implies that this channel contributes at most 1.7% or less to the total decomposition rate constant for temperatures of 2000 K or lower. Furthermore, reaction (R4) also results in the formation of one hydrogen atom for each DME molecule destroyed and so would have essentially no effect on the measured branching ratio.

Reaction (R5) results first in the formation of a long-range complex between $^1CH_2$ and CH_3OH. This complex lies 14 kcal/mol below $^1CH_2 + CH_3OH$ and 1 kcal/mol below the $CH_3O + CH_3$ asymptote. However, the barrier to formation of this complex from DME is predicted to lie 1 kcal/mol above the $CH_3O + CH_3$ asymptote. The possibility of an isomerization of DME to ethanol via the $CH_3OH\cdots^1CH_2$ complex was also considered. The transition

state for this process is predicted to lie 11 kcal/mol above the $CH_3O + CH_3$ asymptote (see Table 4). The high pressure rate constant for formation of the $CH_3OH\cdots^1CH_2$ complex is less than 0.5% of the total decomposition rate constant at 2000 K. Thus, both (R5) and the isomerization process to ethanol will not contribute significantly for the range of temperature and pressure studied experimentally.

The transition state for reaction (R6) is only 1 kcal/mol above that for (R1). However, this 1, 1 elimination transition state is very tight with low entropy. As a result, the maximum contribution to the high pressure decomposition rate from this channel is predicted to be less than 0.4% for temperatures of 2000 K and lower.

The contributions from each of these channels will be greatly reduced away from the high pressure limit. For example, for
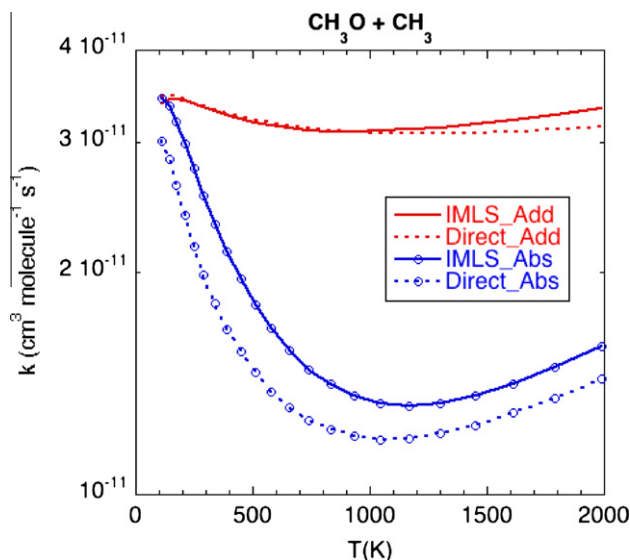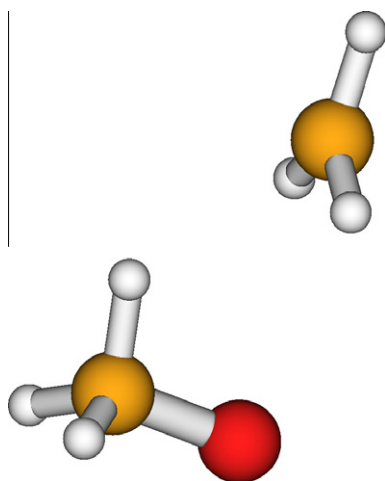
Fig. 13. Plot of the calculated high pressure rate coefficients for addition and abstraction employing either directly sampled ab initio data (dashed lines) or the IMLS potential (solid lines). Both calculations also include the "one-dimensional" corrections. The red lines are for the addition reaction while the blue lines are for the abstraction reaction. (For interpretation of the references to color in this figure legend, the reader is referred to the web version of this article.)

Fig. 14. Structure of the saddle point for the roaming-radical pathway.

Table 4
Calculated CCSD(T)/CBS//CCSD(T)/aug-cc-pvdz energies relative to DME for the stationary points on the C_2H_6O potential surface.

Species	Energy[a] (kcal/mol)
$CH_3 + CH_3O$	90.7 (82.5)
$H_2CO + CH_4$	4.1 (−1.1)
$H + CH_3OCH_2$	103.4 (94.9)
$CH_3OH + {}^1CH_2$	103.5 (96.3)
$CH_3OCH + H_2$	80.0 (70.7)
$CH_3OH–{}^1CH_2$	84.0 (82.0)
$CH_3OCH_3 \rightarrow CH_3OH–{}^1CH_2$	88.1 (83.8)
$CH_3OCH_3 \rightarrow CH_3OCH + H_2$	91.2 (84.2)
$CH_3CH_2OH \rightarrow CH_3OH–{}^1CH_2$	99.1 (93.4)

[a] Numbers in parenthesis include zero point.
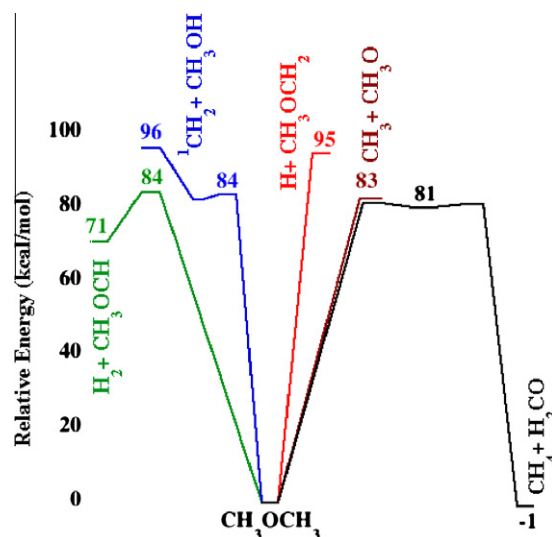
Fig. 15. Schematic of the energetics for the pathways for decomposition of DME.

$H + CH_3OCH_2$ this maximum contribution is reduced to 0.01% at the experimental pressure of ~1 atm. In summary, it is clear that none of these channels will have a significant bearing on the observed branching ratios.

4.2.4. Roaming dynamics

The results of the RDT predictions of the roaming and radical fluxes on the corrected CH_3OCH_3 PES described in Section 3 are reported in Fig. 16. The energy E in the figure is measured with respect to the dissociation threshold for R1 ($E = 0$). The range of the energy E and the transitional mode sum of states $N(E)$ are almost identical to the results of CH_3CHO reported in Fig. 12 of Ref. [17]. (Those results are reproduced in Fig. 16.) Qualitatively the roaming $N(E)$ in CH_3OCH_3 is similar to that in CH_3CHO, but the dissociative $N(E)$ is systematically larger and growing increasingly larger with increasing energy relative to that in CH_3CHO. At a more quantitative level, for energies below the dissociation threshold, the roaming $N(E)$ for CH_3OCH_3 is systematically larger than that in CH_3CHO

as a consequence, as noted earlier, of the more negative roaming saddle point energy.

The corrections for geometry relaxation, zero-point energy changes in conserved modes, and basis set saturation are very significant, even more so than in CH_3CHO. For example, the calculations at an energy of 4 kcal on the *uncorrected* PES show that the roaming $N(E)$ is typically lower by a factor of ~20 relative to the corrected PES while the dissociative $N(E)$ is typically higher by a factor of ~1.5. On CH_3CHO at the same energy, roaming was a factor of five reduced on the *un*corrected relative to the corrected PES. We have represented the corrections with only a few local calibration calculations (see Fig. 1) interpolated globally in a reasonable but not rigorous way. Sample calculations with a variety of alternative correction potentials employing different interpolation schemes yield small variations. In particular, the predicted $N(E)$ for the dissociation channel is essentially independent of the interpolation form while the predicted roaming $N(E)$ can vary up to a factor of two. The largest variations occur in the roaming threshold region where the different forms resulted in substantially different roaming saddle point energies. Such low energy variations tend to have an insignificant effect on the predicted thermal kinetics because the reaction occurs at energies where the rate constant is comparable to the collision timescale, i.e., near the threshold and above for this reaction. Qualitatively, the present three cut representation appears to be reasonably converged but in future work we will provide a more complete examination of these corrections.

The larger transitional mode dissociative flux for CH_3OCH_3 than for CH_3CHO is related to the fact that the approach of CH_3 to the O
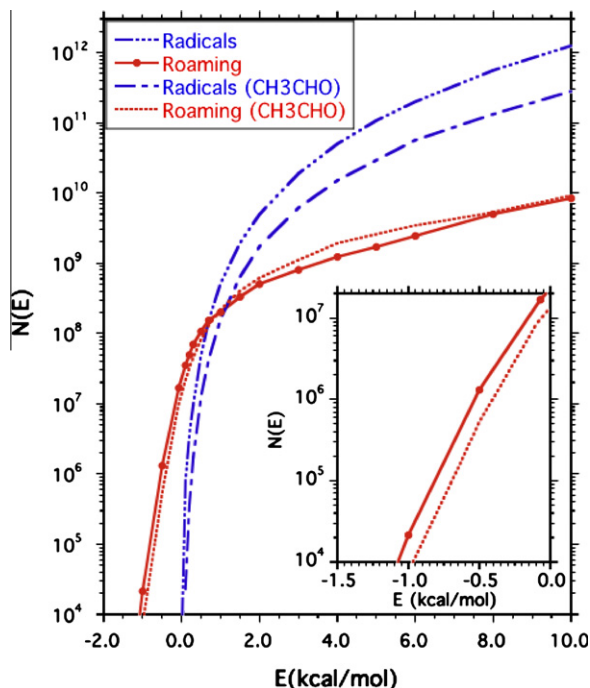
Fig. 16. Calculated sum of states $N(E)$ for the six transitional degrees of freedom versus energy E. Results for dissociation to radicals are indicated in blue while results for roaming are indicated in red. For acetaldehyde, the results are identical to Ref. [17] and are reproduced here for comparison. The insert is a blowup of the results for $E < 0$. The dots indicate the specific energies at which flux calculations were carried out. (For interpretation of the references to color in this figure legend, the reader is referred to the web version of this article.)

end of CH_3O is highly attractive for the full range of HCOC torsional angles. In contrast, the approach of CH_3 to HCO corresponds to a strongly attractive formation of CH_3CHO only for in-plane attack from one side of the HCO group. As a result the entropic reduction of the flux is greater for the CH_3CHO dissociation and this reduction increases with increasing energy as the transition state moves to closer separations.

The larger roaming flux for CH_3OCH_3 than for CH_3CHO for $E < 0$ is also not surprising, given that the saddle point barrier for roaming in CH_3CHO is ~-1.0 kcal/mol, about 0.6 kcal/mol higher than in CH_3OCH_3. However, for $E > 0$, the roaming flux is surprisingly similar between the two systems. To confirm the consistency of the IMLS based PES with the method previously applied to CH_3CHO, an analogous IMLS PES was calculated for CH_3CHO and the RDT method was applied to produce roaming and dissociative $N(E)$ at selected energies. Although this will be the subject of a more comprehensive paper in the future, we note here that the resulting values of the dissociative and roaming $N(E)$ differ by less than 15% at $E = 3$ and 10 kcal/mol from the published results [17] on a non-IMLS PES.

4.3. DME decomposition kinetics: comparison of theory and experiment

The results for k_1 from Tables 2 and 3 and the theoretical predictions from the present work are compared in Figs. 17 and 18 to earlier decomposition studies [4–10] at high and low temperature, respectively. The data in Tables 2 and 3 are represented in both figures (and also Fig. 19) but for clarity, the different pressures are binned into groups. The pressures represented in each single density group in Table 2 vary by <10% about the mean value of the bin. If the data from Tables 2 and 3 together are considered, the dispersion increases marginally to about ±15% from the mean
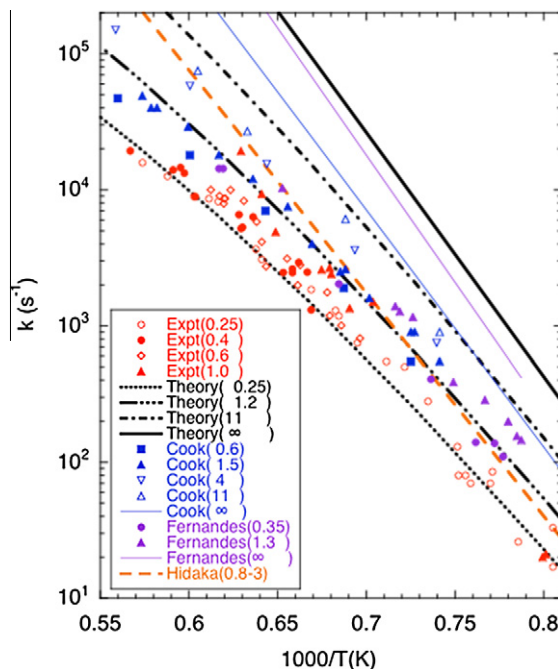

Fig. 17. First order rate constants for $CH_3OCH_3 \rightarrow CH_3O + CH_3$ at high temperature and for the pressures (bar) listed in parentheses. Red symbols – present data, blue symbols and line – Cook et al. [10], purple symbols and line– Fernandes et al. [9], orange dashed line – Hidaka et al. [8], black lines – present theory. (For interpretation of the references to color in this figure legend, the reader is referred to the web version of this article.)
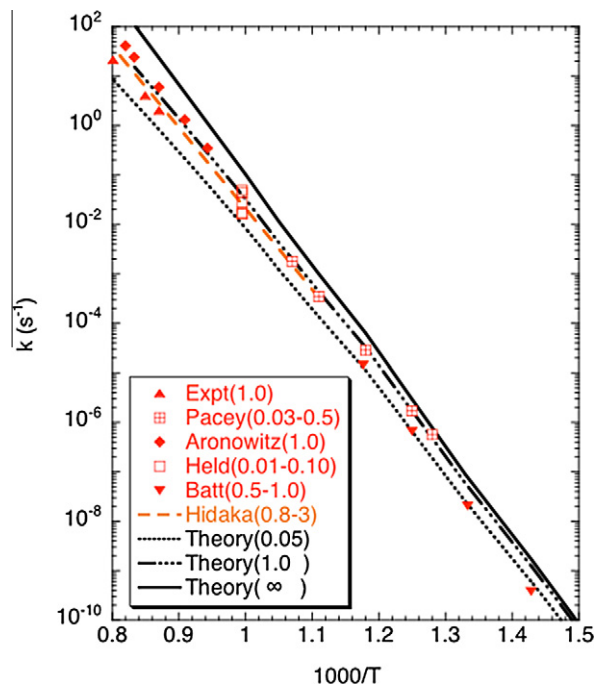

Fig. 18. First order rate constants for $CH_3OCH_3 \rightarrow CH_3O + CH_3$ at low temperature and for the pressures (bar) listed in parentheses. Open circles– present data, thatched square – Pacey [4], solid diamond – Aronowitz and Naegeli [5], open squares – Held et al. [6], downward solid triangle – Batt et al. [7], orange dashed line – Hidaka et al. [8]; black lines – present theory. (For interpretation of the references to color in this figure legend, the reader is referred to the web version of this article.)

value. In Fig. 17, the present measurements in the highest pressure bin (1.0 bar) are in reasonable agreement with the two recent high-
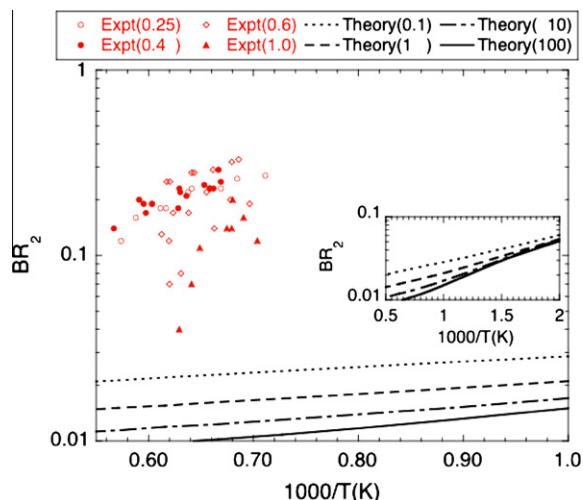
Fig. 19. Experimentally measured and theoretical predicted roaming branching ratio as a function of inverse temperature with pressure (bar) listed in parentheses. Insert plot is for theory alone over the extend temperature range of all DME kinetics measurements.

temperature studies by Fernandes et al. [9] and Cook et al. [10] at comparable pressures (1.3 and 1.5 bar, respectively). The observed fall-off however is more severe at the lowest-P of the present study in comparison to these two recent studies. At the lowest pressures (0.25 bars) the present data for k_1 are lower by a factor of 2 than the two recent measurements [9,10] over similar pressure ranges. In the case of Fernandes et al. [9], the discrepancy might be attributed to the T-invariant choice for k_3 when modeling their [H] profiles. On the other hand, the OH-absorption measurements of Cook et al. [10] are sensitive to a number of abstraction reactions, DME + OH and DME + H, apart from H + $O_2 \rightarrow$ O + OH, and consequently required using a detailed model to extract k_1 and this might be a reason for the observed discrepancies with the present data. The representation of Hidaka et al., which ignores the dependence on pressure, is reasonably concordant with the present data.

The theoretical predictions for k_1, which employ a fitted $\langle \Delta E_{down} \rangle$, accurately reproduce the experimental data presented in this paper. They also provide a satisfactory representation of the low temperature data from [4–7], particularly when one considers the predicted deviations from the high pressure limit. Furthermore, they are reasonably representative of the data of Cook et al. [10] and Fernandes et al. [9], although, as noted above, there are deviations of about a factor of 2 toward lower pressures. Over the whole temperature range in Fig. 17, the present theoretical prediction for the high pressure limit is slightly larger than that derived by Fernandes et al. [9] and larger by a factor of 3–4 than that derived by Cook et al. [10]. The present theoretical predictions are well reproduced over the 500–2000 K temperature range and the 0.01–300 bar pressure range by the following modified Arrhenius parameters for the Troe falloff format:

$$k_{1,\infty}(T) = 2.33 \times 10^{19} T^{-0.661} \exp(-42345/T) \text{ s}^{-1}$$

$$k_{1,0}(T) = 2.86 \times 10^{35} T^{-11.4} \exp(-46953/T) \text{ cm}^3 \text{ molecule}^{-1} \text{ s}^{-1}$$

$$F_{cent}(T) = \exp(-T/880)$$

Figure 19 provides a comparison of the temperature and pressure dependence of the present theoretical predictions for the roaming branching, BR_2, with the experimental measurements. The theoretical prediction of ~0.02 for the experimental conditions

dramatically underestimates the experimentally observed value. As the insert in the figure shows, over the whole range of DME kinetics measurements down to 650 K, the theory predicts an increasing BR_2 with decreasing temperature and pressure, trends that as mentioned above are discernable in the experimental data. However, over the full temperature range, the calculated BR_2 never exceeds 10%, while the measurements are 10 times larger at the high temperatures of 1400–1750 K. It is not clear why this should be the case. There are a number of aspects to the present calculation that could introduce errors, such as inaccuracies in the trajectory propagation, failures of the reduced dimensional framework, inaccuracies in the treatment of energy transfer, the neglect of dynamical effects arising from Jahn–Teller and spin–orbit interactions and, perhaps most notably, inaccuracies of the potential energy surface, especially those related to the "one-dimensional" corrections. Nevertheless, it is hard to envision how any of these inadequacies would yield an order of magnitude increase in the predicted branching ratio.

It is interesting to note that the present RDT-based estimate for BR_2 is even lower than that predicted for the decomposition of CH_3CHO. The magnitude of roaming for the thermal dissociation arises from a convolution of the energy dependent roaming flux (cf. Fig. 16) with the steady state distribution for dissociation. The results in Fig. 16 indicate that, if the threshold region of roaming (i.e., $E < 0$) dominates, BR_2 for CH_3OCH_3 will be larger than that for CH_3CHO. If, instead, the region above the threshold for dissociation (i.e., $E > 0$) dominates, BR_2 for CH_3OCH_3 will be smaller than that for CH_3CHO. At 1500 K, with only a 2 kcal/mol difference in thresholds for roaming as opposed to radical formation, the region above the threshold dominates and BR_2 is larger for CH_3CHO. This discussion also indicates that the smallness of the roaming for DME arises from the very small ratio of the roaming to radical fluxes at high energy. What is not clear is why this ratio should be so much smaller for DME than for CH_3CHO.

5. Conclusions

The contribution of the roaming channel to the total thermal dissociation rate in dimethyl ether is measured to be 0.19 ± 0.07 for temperatures in the range from 1406 to 1764 K and pressures in the range 0.2–1.25 atm. The combination of these measurements with the theoretical analysis provides definitive evidence for a contribution from a roaming radical mechanism in this thermal decomposition, although the theoretical analysis does suggest that this roaming should be an order of magnitude lower. In the studied range there is evidence that the branching ratio has trends with temperature and pressure that are in the same direction as those found in the theoretical analysis.

In contrast, the theoretical predictions for the thermal DME decomposition rate constant for formation of radical products $CH_3 + OCH_3$ accurately reproduced the experimental measurements. Troe format expressions for the temperature and pressure dependence of this rate constant were obtained from the theoretical analysis. The rate coefficient for the CH_3OCH_3 + H reaction was also measured in the present experimental work using more concentrated mixtures than those used in the yield experiments. An evaluation of the data from 273 to 1465 K yields the expression given in Eq. (E3).

This study is the first application of IMLS PES generation for use in an RDT study of roaming. This application illustrates the trade-offs with the IMLS approach. The production level generation of the PES took less than a week with little human intervention and involved ~4000 ab initio calculations generally done in groups of 20 in parallel. This is much faster than generating the PES for CH_3CHO by non-IMLS means where extensive human intervention

and 20 times the number of ab initio calculations were required. However, the resulting non-IMLS CH_3CHO PES involves evaluating only a handful of expansions to obtain an energy on the PES, while the IMLS PES for CH_3OCH_3 involves evaluating one or two orders of magnitude more expansions to obtain an energy. As a result, RDT calculations on the IMLS PES for CH_3OCH_3 took from a day to a week while RDT calculations on the non-IMLS PES for CH_3CHO typically took at most a few hours. In effect, the IMLS approach has greatly reduced human intervention time and shifted computer resource allocations from generation to application. Methods for speeding up IMLS PES evaluations (such as simpler distance metrics or nearest-neighbor lists in trajectory applications) are currently under investigation.

As part of an effort to uncover the origins of the difference in the roaming branching ratio between theory and experiment, we are carrying out further roaming studies on CH_3OCH_3 and also on CH_3CHO and $CH_3C_2H_5$. The global reliability of 1-D correction terms, the impact of local improvements to the PES (e.g., the abstraction region for $CH_3 + OCH_3$), and the limitations of rigid fragment approximations are being investigated.

Acknowledgments

Appendix A. Supplementary material

Supplementary data associated with this article can be found, in the online version, at doi:10.1016/j.combustflame.2010.12.017.

References

[1] http://www.aboutdme.org.
[2] A.L. Boehman, Fuel Process. Technol. 89 (2008) 1243.
[3] Z. Zhao, M. Chaos, A. Kazakov, F.L. Dryer, Int. J. Chem. Kinet. 40 (2008) 1–18.
[4] P.D. Pacey, Can. J. Chem. 53 (1975) 2742–2747.
[5] D. Aronowitz, D. Naegeli, Int. J. Chem. Kinet. 9 (1977) 471–479.
[6] A.M. Held, K.C. Manthorne, P.D. Pacey, H.P. Reinholdt, Can. J. Chem. 55 (1977) 4128–4134.
[7] L. Batt, G. Alvarado-Salinas, I.A.B. Reid, C. Robinson, D.B. Smith, Proc. Combust. Inst. 19 (1982) 81–87.
[8] Y. Hidaka, K. Sato, M. Yamane, Combust. Flame 123 (2000) 1–22.
[9] R.X. Fernandes, C. Fittschen, H. Hippler, React. Kinet. Catal. Lett. 96 (2009) 279–289.
[10] R.D. Cook, D.F. Davidson, R.K. Hanson, J. Phys. Chem. A 113 (2009) 9974–9980.
[11] L.B. Harding, S.J. Klippenstein, J. Phys. Chem. Lett. 1 (2010) 3016–3020.
[12] D. Townsend, S.A. Lahankar, S.K. Lee, S.D. Chambreau, A.G. Suits, X. Zhang, J.L. Rheinecker, L.B. Harding, J.M. Bowman, Science 306 (2004) 1158–1161.
[13] P.L. Houston, S.H. Kable, Proc. Natl. Acad. Sci. 103 (2006) 16079–16082.
[14] B.R. Heazlewood, M.J.T. Jordan, S.H. Kable, T.M. Selby, D.L. Osborn, B.C. Shepler, B.J. Braams, J.M. Bowman, Proc. Natl. Acad. Sci. 105 (2008) 12719–12724.
[15] B.S. Shepler, B.J. Braams, J.M. Bowman, J. Phys. Chem. A 112 (2008) 9344–9351.
[16] R. Sivaramakrishnan, J.V. Michael, S.J. Klippenstein, J. Phys. Chem. A 114 (2010) 755–764.
[17] L.B. Harding, Y. Georgievskii, S.J. Klippenstein, J. Phys. Chem. A 114 (2010) 765–777.
[18] (a) R. Dawes, A.F. Wagner, D.L. Thompson, J. Phys. Chem. A 113 (2009) 4709–4721;
(b) R. Dawes, D.L. Thompson, A.F. Wagner, M. Minkoff, J. Chem. Phys. 128 (2008) 084107;
(c) R. Dawes, D.L. Thompson, Y. Guo, A.F. Wagner, M. Minkoff, J. Chem. Phys. 126 (2007) 184108;
(d) Y. Guo, I. Tokmakov, D.L. Thompson, A.F. Wagner, M. Minkoff, J. Chem. Phys. 127 (2007) 214106.
[19] J.V. Michael, A. Lifshitz, in: G. Ben-Dor, O. Igra, T. Elperin, A. Lifshitz (Eds.), Handbook of Shock Waves, vol. 3, Academic Press, New York, 2001, pp. 77–105.
[20] S.S. Kumaran, J.J. Carroll, J.V. Michael, Proc. Combust. Inst. 27 (1998) 125–133.
[21] K. Takahashi, O. Yamamoto, T. Inomata, M. Kogoma, Int. J. Chem. Kinet. 39 (2007) 97–108.
[22] J.V. Michael, Prog. Energy Combust. Sci. 18 (1992) 327–347.
[23] J.V. Michael, in: J.R. Barker (Ed.) Advances in Chemical Kinetics and Dynamics, vol. I, JAI, Greenwich, 1992, pp. 47–112.
[24] J.V. Michael, J.W. Sutherland, Int. J. Chem. Kinet. 18 (1986) 409–436.
[25] J.V. Michael, J. Chem. Phys. 90 (1989) 189–198.
[26] J.V. Michael, J.R. Fisher, in: Y.W. Kim (Ed.), Seventeenth International Symposium on Shock Waves and Shock Tubes, AIP Conference Proceedings, vol. 208, American Institute of Physics, New York, 1990, p. 210.
[27] S.S. Kumaran, J.J. Carroll, J.V. Michael, Proc. Combust. Inst. 27 (1998) 125–133.
[28] K.P. Lim, J.V. Michael, Proc. Combust. Inst. 25 (1994) 713–719 (and references therein).
[29] S.S. Kumaran, M.-C. Su, K.P. Lim, J.V. Michael, Proc. Combust. Inst. 26 (1996) 605–611.
[30] R.G. Maki, J.V. Michael, J.W. Sutherland, J. Phys. Chem. 89 (1985) 4815–4821.
[31] H.-J. Werner, Mol. Phys. 89 (1996) 645–661.
[32] P. Celani, H.-J. Werner, J. Chem. Phys. 112 (2000) 5546–5557.
[33] H.-J. Werner, P.J. Knowles, R. Lindh, F.R. Manby, M. Schütz, P. Celani, T. Korona, A. Mitrushenkov, G. Rauhut, T.B. Adler, R.D. Amos, A. Bernhardsson, A. Berning, D.L. Cooper, M.J.O. Deegan, A.J. Dobbyn, F. Eckert, E. Goll, C. Hampel, G. Hetzer, G. Knizia, C. Köppl, Y. Liu, A. W. Lloyd, R.A. Mata, A.J. May, S.J. McNicholas, W. Meyer, M.E. Mura, A. Nicklaß, P. Palmieri, K. Pflüger, R. Pitzer, M. Reiher, U. Schumann, H. Stoll, A. J. Stone, R. Tarroni, T. Thorsteinsson, M. Wang, A. Wolf, MOLPRO, Version 2009.1, a package of ab initio programs. <www.molpro.net>.
[34] R. Dawes, X.-G. Wang, A.W. Jasper, T. Carrington Jr., J. Chem. Phys. 133 (2010) 134304.
[35] (a) I.M. Sobol, USSR Comput. Maths. Math. Phys. 16 (1976) 236–242. in English;
(b) W.H. Press, S.A. Teukolsky, W.T. Vetterling, B.P. Flannery, Numerical Recipes in Fortran 77: The Art of Scientific Computing, second ed., Cambridge University Press, Cambridge, UK, 1992.
[36] R.N. Zare, Angular Momentum, Wiley, New York, 1988.
[37] J.A. Miller, S.J. Klippenstein, J. Phys. Chem. A 110 (2006) 10528–10544.
[38] A.W. Jasper, J.A. Miller, J. Phys. Chem. A 113 (2009) 5612–5619.
[39] A.E. Lutz, R.J. Kee, J.A. Miller, SAND87-8248 Revised, Sandia National Laboratory, November 1997.
[40] R.S. Tranter, R.W. Walker, Phys. Chem. Chem. Phys. 3 (2001) 4722–4732.
[41] C. Faubel, K. Hoyermann, E. Stroger, H. Gg. Wagner, Ber. Bunsen – Ges. Phys. Chem. 83 (1979) 532.
[42] J.H. Lee, R.C. Machen, D.F. Nava, L.J. Stief, J. Chem. Phys. 74 (1981) 2839–2844.
[43] J.F. Meagher, P. Kim, J.H. Lee, R.B. Timmons, J. Phys. Chem. 78 (1974) 2650–2657.
[44] F. Slemr, P. Warneck, Int. J. Chem. Kinet. 9 (1977) 267–282.
[45] J.Y. Wu, J. Y Liu, Z.S. Li, X.R. Huang, C.C. Sun, J. Comput. Chem. 24 (2003) 593–600.
[46] Q.S. Li, Y. Zhang, S.W. Zhang, J. Phys. Chem. A 108 (2004) 2014–2019.
[47] L.N. Krasnoperov, E.N. Chesnokov, H. Stark, A.R. Ravishankara, J. Phys. Chem. A 108 (2004) 11526–11536.
[48] N.K. Srinivasan, M.-C. Su, J.W. Sutherland, J.V. Michael, J. Phys. Chem. A 109 (2005) 7902–7914.